# Impact of stratospheric aerosol intervention geoengineering on surface air temperature in China: A surface energy budget perspective

Zhaochen Liu[1, 4], Xianmei Lang[1, 2, 3], and Dabang Jiang[1, 3, 4*]

[1]Institute of Atmospheric Physics, Chinese Academy of Sciences, Beijing 100029, China

[2]Collaborative Innovation Center on Forecast and Evaluation of Meteorological Disasters, Nanjing University of Information Science and Technology, Nanjing 210044, China

[3]CAS Center for Excellence in Tibetan Plateau Earth Sciences, Beijing 100101, China

[4]College of Earth and Planetary Sciences, University of Chinese Academy of Sciences, Beijing 100049, China

*Correspondence to*: Dabang Jiang (jiangdb@mail.iap.ac.cn)

**Abstract.** Stratospheric aerosol intervention (SAI) geoengineering is a proposed scheme to counteract anthropogenic global warming, but the climate response to SAI, with great regional disparities, remains uncertain. In this study, we use Geoengineering Model Intercomparison Project G4 experiment simulations from six models that counteract anthropogenic forcing under medium-low emissions (RCP4.5) by injecting a certain amount of $SO_2$ into the stratosphere every year, to investigate the surface air temperature response to SAI geoengineering over China. We have found that SAI leads to surface cooling over China during the last 40 years of injection simulation (2030–2069), which varies among models, regions and seasons. Decreased tropospheric temperature and water vapor and increased stratospheric aerosols induce robust decreases in downward clear-sky longwave and shortwave radiation fluxes at the surface respectively, dominating the temperature change over China. Changes in cloud effective forcing and surface albedo feedback also relate to the temperature response, but with large spatial and seasonal variations. We find that the increased summer cloud cover and winter surface albedo lead to strong cooling, while the decreased summer cloud cover and winter surface albedo lead to weak cooling or even warming for the certain subregions and models. Our results suggest that cloud and land surface processes in models dominate the spatial pattern of SAI-induced surface air temperature change over China.

## 1 Introduction

The increasing anthropogenic greenhouse gas (GHG) concentrations since the industrial revolution have led to global warming. Although the international community has realized the risk of global warming and attempted to reduce GHG emissions, global GHG emissions still show a continuous increase (United Nations Environment Programme, 2020). The "2°C global temperature target" in the Paris Agreements will be unachievable if the current increasing emission trend persists (e.g., Robiou du Pont and Meinshausen 2018). Solar radiation modification (SRM), which refers to a range of measures adjusting the Earth's radiative balance, is considered as an option to counteract anthropogenic global warming. Various specific techniques have been proposed to perform SRM geoengineering, such as injecting sulfate aerosols into the stratosphere (Budyko, 1977), placing shields or deflectors in space (Seifritz, 1989), brightening marine clouds (Latham, 1990), and thinning cirrus clouds (Mitchell and Finnegan, 2009). The method of injecting sulfate aerosols or their precursors into

40  the stratosphere, also known as stratospheric aerosol intervention (SAI) geoengineering, is designed to

41  cool the surface by using these aerosols to reflect and scatter solar radiation (Crutzen, 2006; Wigley,

42  2006). As a proposed scheme, SAI has attracted great attention recently due to its assumed

43  technological feasibility (e.g., Irvine et al., 2016).

44      SRM geoengineering has not been implemented in reality because of its potential risks and

45  immature technology. The primary means of recognizing the climate response to geoengineering is

46  simulating via general circulation models (GCMs). However, the results from early simulations could

47  not be proved robust due to the differences in experimental schemes. The Geoengineering Model

48  Intercomparison Project (GeoMIP) has been proposed to address that issue (Kravitz et al., 2011; 2015).

49  To date, the GeoMIP has designed 12 experiments, including solar dimming, stratospheric aerosol

50  intervention, marine cloud brightening, and cirrus thinning geoengineering in Coupled Model

51  Intercomparison Project Phases 5 and 6 (CMIP5 and CMIP6). The GeoMIP provides detailed

52  guidelines for each model and experiment and calls for all the modeling groups worldwide to become

53  involved and share their simulations. A total of 19 GCMs have participated in the GeoMIP to date.

54  More    detailed    information    is    accessible    from    the    GeoMIP    website

55  (http://climate.envsci.rutgers.edu/GeoMIP/).

56      Previous studies have indicated that SRM geoengineering could counteract or even reverse

57  anthropogenic global warming and reduce sea ice melting and thermosteric sea-level rise, as well as

58  decrease the frequency and intensity of extreme temperature and precipitation events (Rasch et al.,

59  2008; Robock et al., 2015; Irvine et al., 2016; Ji et al., 2018; Jones et al., 2018). It might also come

60  with risks. For instance, SRM geoengineering would reduce the global mean precipitation and

61  monsoon precipitation and slow the hydrological cycle if it is used to offset the GHG-induced global

62  warming (Bala et al., 2008; Tilmes et al., 2013; Sun et al., 2020). SRM would not mitigate the

63  continued ocean acidification caused by $CO_2$ emissions (Caldeira et al., 2013). The sudden termination

64  of geoengineering would lead to a more rapid increase in temperature than the non-geoengineered case

65  (Matthews and Caldeira, 2007; Jones et al., 2013). The severity of the termination effect depends on

66  the magnitude of geoengineering deployment. Moreover, the SAI-induced heterogeneous chemistry

67  changes might cause stratospheric ozone depletion and thus increase ultraviolet radiation (UV) at the

68  surface (Tilmes et al., 2008; Eastham et al., 2018).

69      The appropriate SRM geoengineering might lead to global cooling and benefit most regions

70    (Irvine et al., 2019). However, it was still a concern that some regions might face greater climatic

71    impacts or risks under SRM forcing (Ricke et al., 2013; Kravitz et al., 2014). For example, Robock et

72    al. (2008) indicated that the weakening of the Asian and African summer monsoons caused by the

73    injected stratospheric aerosols over the Arctic would decrease cloudiness and in turn warm the surface

74    over northern Africa and India. In addition to the effect of cloudiness, changes in atmospheric moisture

75    and surface conditions caused by SAI also impact surface air temperature (Kashimura et al., 2017). As

76    the largest developing country in the world, China plays an important role in combating climate change.

77    China's attitude to SAI is crucial to the international geoengineering research community. Considering

78    the combined effect of the Tibetan Plateau and the East Asian monsoon, the climate over China would

79    be strongly influenced by SAI. Large volcanic eruptions, which inject massive volcanic aerosols into

80    the stratosphere, are considered a natural analog to SAI geoengineering (Trenberth and Dai, 2007).

81    The 1815 Mt. Tambora eruption led to the "year without a summer" over China (e.g., Raible et al.,

82    2016). But the volcanic eruption is not a perfect analog. This is because the sulfate aerosols from

83    massive volcanic eruptions only last for 2–3 years, while the SAI-induced aerosols are continuously

84    replenished for decades or centuries (Duan et al., 2019). So far, few studies have studied the

85    temperature response to SAI geoengineering over China explicitly (Cao et al., 2015).

86        In this study, we investigate the impact of the SAI geoengineering on the surface air temperature

87    over China and the underlying physical processes from a surface energy perspective. Section 2

88    provides a brief introduction to the experiments, model data, and decomposition method of surface air

89    temperature change. Section 3 evaluates the ability of models to reproduce the climatological

90    temperature over China in summer and winter. Section 4 presents the summer and winter temperature

91    changes and associated reasons over China in response to SAI geoengineering, and we also analyze

92    the physical processes responsible for the SAI-induced temperature changes over China. Conclusions

93    and discussion are presented in Sect. 5.


94    **2 Experiments, data, and methods**


95    **2.1 Experiments**


96        We use the G4 experiment from the first phase of the GeoMIP (Kravitz et al., 2011). As a SAI-

based geoengineering experiment, G4 is designed to inject $SO_2$ into the low-level equatorial stratosphere at a consistent rate of 5 Tg per year under the background scenario of Representative Concentration Pathway 4.5 (RCP4.5) (Taylor et al., 2012). This injection rate is equivalent to a case in which the 1991 Mt. Pinatubo eruption occurred every four years (Bluth et al., 1992). The injection period is from 2020 to 2069, and then the experiment continues to run until 2089 to examine the termination effect (Jones et al., 2013). The RCP4.5 simulation for the same period is used as a baseline (non-geoengineered) state. In addition, the historical simulation for 1986–2005 is applied to evaluate the ability of the selected models to reproduce the climatology of surface air temperature over China.

**2.2 Data**

A total of 12 GCMs participated in the G4 experiment (Kravitz et al., 2013a). However, some models should not be considered in this study due to their known issues. For instance, CSIRO-Mk3L-1-2 runs G4 by directly reducing solar irradiance rather than injecting stratospheric aerosols; GISS-E2-R shows an inconsistency between G4/RCP4.5 and historical experiments; IPSL-CM5A-LR and NorESM1-M have errors in the longwave treatment of the sulfate aerosol; GEOSCCM and ULAQ use prescribed sea surface temperatures. Simulations from the other six models are applied for analyses. Monthly datasets are used and calculated as the averages in summer (June–July–August, JJA) and winter (December–January–February, DJF). The CN05.1 observation dataset (Wu and Gao, 2013) is used to evaluate the ability of models to reproduce the climatology of temperature over China. All the observations and model outputs are interpolated to a common grid with a mid-range horizontal resolution (2.5° longitude by 2° latitude).

A brief description of the selected models is illustrated in Table 1. In addition to differences in the physical and chemical modules related to sulfate aerosol particles, the models have different $SO_2$ injection treatments. For HadGEM2-ES, the CLASSIC aerosol module (Bellouin et al., 2011) used in the stratosphere makes it possible to handle the injections of $SO_2$, allowing HadGEM2-ES to finish a complete simulation including the generation and transportation of stratospheric sulfate aerosols. The injection point is located on the equator (0° longitude), and the injection altitude ranges from 16 to 25 km. For CanESM2, the stratospheric aerosol optical depth (SAOD) caused by SAI is prescribed as a consistent value. For other models (BNU-ESM, CNRM-ESM1, MIROC-ESM and MIROC-ESM-CHEM), the prescribed distribution of SAOD, according to Sato (2006), is used to drive the G4

126    experiment. Besides, MIROC-ESM-CHEM calculates the surface density of sulfate aerosols by using

127    the CHASER atmospheric chemistry module (Sudo et al., 2002; Kravitz et al., 2013a).

**2.3 Decomposition method for SAI-induced surface air temperature change**

129        Surface air temperature is a widely used variable in climate studies. Change in surface air

130    temperature is associated with three components: surface vertical energy fluxes (including radiative

131    and heat fluxes), horizontal temperature advection, and adiabatic warming or cooling (Gong et al.,

132    2017). In this study, the SAI-induced changes in surface temperature and surface air temperature are

133    strongly coupled in China during 2030–2069 (the correlation coefficients are higher than 0.98 and 0.99

134    in summer and winter, respectively; Fig. 1). Thus, the surface vertical energy fluxes are considered to

135    be the main factor affecting temperature change under SAI forcing.

136        According to the decomposition method based on the surface energy budget proposed by Lu and

137    Cai (2009), the surface air temperature change caused by SAI can be written as:

138
$$\Delta T = \frac{\Delta R^{\downarrow} + \Delta\text{LH} + \Delta\text{SH} + \Delta Q}{4\sigma\overline{T_s}^3} + \text{Res} \tag{1}$$

139    where $\Delta$ represents the difference between G4 and RCP4.5, the overbar represents the climatological

140    value of RCP4.5, $R^{\downarrow}$ is the downward net radiation at the surface, LH and SH are surface sensible and

141    latent heat fluxes respectively, $Q$ is surface heat storage, $T_s$ is surface temperature, and $\sigma$ is the Stefan-

142    Boltzmann constant. Res represents the difference between changes in surface air temperature and

143    surface temperature. In order to quantitatively separate the radiative effects of clouds and surface

144    albedo, the $\Delta R^{\downarrow}$ can be decomposed as follow:

145
$$\Delta R^{\downarrow} = \Delta\text{LW}^{\text{cs}\downarrow} + (1-\overline{\alpha})\Delta\text{SW}^{\text{cs}\downarrow} + \Delta\text{SAF} + \Delta\text{CRF} \tag{2}$$

146
$$\Delta\text{SAF} = -(\Delta\text{SW}^{\text{as}\downarrow} + \overline{\text{SW}^{\text{as}\downarrow}})\Delta\alpha \tag{3}$$

147
$$\Delta\text{CRF} = (1-\overline{\alpha})\Delta\text{SW}^{\text{cl}\downarrow} + \Delta\text{LW}^{\text{cl}\downarrow} \tag{4}$$

148        In Eqs. (2)–(4), $\text{SW}^{\text{as}\downarrow}$ represents downward surface shortwave radiation in all-sky conditions,

149    $\text{SW}^{\text{cs}\downarrow}$ and $\text{LW}^{\text{cs}\downarrow}$ represent downward surface shortwave and longwave radiations in clear-sky

150    conditions respectively, $\text{SW}^{\text{cl}\downarrow}$ and $\text{LW}^{\text{cl}\downarrow}$ represent downward shortwave and longwave radiative

151    effects of clouds (all-sky radiations minus clear-sky radiations) respectively, and $\alpha$ represents surface

albedo (the ratio of solar radiation reflected to the atmosphere at the surface). SAF is surface albedo feedback, and CRF is cloud radiative forcing. Under SAI forcing, both the changes in atmospheric reflection and atmospheric absorption affect the $SW^{cs\downarrow}$. We assume that the clear-sky atmospheric reflection change is only affected by atmospheric water vapor amount, and the clear-sky atmospheric absorption change is only affected by the aerosol scattering effect. As detailed by Kashimura et al. (2017), the change in $SW^{cs\downarrow}$ can be further decomposed as:

$$\Delta SW^{cs\downarrow} \approx \Delta SW_{SRM} + \Delta SW_{WV} \tag{5}$$

$$\Delta SW_{SRM} = SW^{cs\downarrow}(F_{G4}^{cs}, A_{RCP}^{cs}) - \overline{SW^{cs\downarrow}} \tag{6}$$

$$\Delta SW_{WV} = SW^{cs\downarrow}(F_{RCP}^{cs}, A_{G4}^{cs}) - \overline{SW^{cs\downarrow}} \tag{7}$$

where $F$ is the fraction of solar radiation reflected by the atmosphere, and $A$ is the fraction of absorption during solar radiation passing through the atmosphere. $SW_{SRM}$ and $SW_{WV}$ represent the effects of solar radiation scattering and atmospheric water vapor amount, respectively. Although the $SW^{cs\downarrow}$ change is not precisely equal to the sum of changes in $SW_{SRM}$ and $SW_{WV}$ due to the assumption of a single-layer model (Donohoe and Battisti, 2011), this method is effective when analyzing the surface shortwave radiation change in response to SAI (Kashimura et al., 2017).

## 3 Evaluation of the models

The ability of the models to reproduce the surface air temperature over China is evaluated first. As shown in Fig. 2, the spatial correlation coefficient (SCC), standard deviation (SD), and centered root-mean-square error (CRMSE) between the observation and the historical simulation for climatological temperature over China during 1986–2005 are calculated and illustrated in a Taylor diagram (Taylor, 2001). The SCCs of the models range from 0.85 to 0.95 (0.94 in multi-model mean) in summer and from 0.91 to 0.96 (0.96 in multi-model mean) in winter. All the SCCs are statistically significant at the 99% level, meaning that the simulated temperature is in good agreement with the observed temperature. The normalized SDs range from 0.81 to 1.33 in summer (0.99 in multi-model mean) and from 1.03 to 1.23 (1.08 in multi-model mean) in winter. This result indicates that all selected models overestimate the spatial variability of the winter temperature in China. The CRMSEs are 0.34–0.53 (0.35 in multi-model mean) for summer and 0.32–0.46 (0.31 in multi-model mean) for

179     winter. Taken together, the simulations of summer and winter temperatures by selected models are

180     reliable over China. The multi-model mean results outperform most individual models for the

181     temperature climatology over China both in summer and winter, which is consistent with previous

182     findings (e.g., Jiang et al., 2016).

183         The observed spatial patterns of summer and winter temperature climatology over China show

184     a general decrease from south to north, and the lowest values mainly occur in the Tibetan Plateau

185     (Figs. 3a, d). These features can be well reproduced by all models and their mean (Figs. 3b, e).

186     Compared to the observation, the simulated temperature is generally overestimated in summer but

187     underestimated in winter over China according to the regionally averaged values. In summer, warm

188     biases occur in most of eastern China, especially in northeastern China (Fig. 3c). In winter, however,

189     the underestimation of temperature exists at the national scale, with a regionally averaged cold bias

190     of 1.79°C in multi-model mean (Fig. 3f). Substantial cold biases occur over the Tarim Basin and the

191     Tibetan Plateau, which are associated with regional topography. Most of the above biases are

192     consistent among individual models, with the averaged model consistency of 76% over China in both

193     summer and winter.

194     **4 Results**

195     **4.1 Changes in surface air temperature over China**

196         Figures 4 and 5 show the temporal evolution of surface air temperature changes in the G4

197     experiment and RCP4.5 scenario relative to the present climatology (1986–2005) over China. Both the

198     summer and winter temperatures in G4 increase over time, although they are colder than those in

199     RCP4.5. Positive values occur throughout the whole G4 simulation period, excluding several years in

200     winter. This indicates that although the injection of 5 Tg $SO_2$ per year leads to a surface cooling over

201     China, the climatological temperature in G4 is still higher than the present level. Considering that the

202     feedback response timescale of diffusive ocean heat uptake in climate models is approximately ten

203     years (Jarvis, 2011), the simulation representing the last 40 years of injection (2030–2069) is used to

204     examine the temperature response to SAI over China, as done by Kravitz et al. (2013b) and Tilmes et

205     al. (2013). During this period, the warming trends over all of China in G4 among models are 0.21–

0.43°C decade$^{-1}$ in summer and 0.30–0.59°C decade$^{-1}$ in winter. It can be seen that the warming trend difference between G4 and RCP4.5 is small, and this is expected because of the similar trend of radiative forcing variation in the two experiments during 2030–2069. The regionally averaged temperature over China is decreased by 0.24–0.96°C (0.64°C in the multi-model mean) in summer and 0.30–1.52°C (0.80°C in the multi-model mean) in winter due to SAI forcing. Although the magnitude of SAI-induced temperature change varies across models and seasons, the cooling response is consistent among models over China. The winter cooling is stronger than the summer level in all models. Additionally, the result shows the strongest SAI-induced cooling occurs in HadGEM2-ES in both summer and winter.

The spatial pattern of the temperature difference between G4 and RCP4.5 over China is illustrated in Figs. 6 and 7. The multi-model results show a robust and coherent cooling in both summer and winter. Strong cooling with magnitudes greater than 0.8°C mainly occurs over high-latitude regions, including northwestern and central China. For the individual models, the SAI-induced temperature changes are negative and significant almost everywhere over China except for in MIROC-ESM and MIROC-ESM-CHEM. SAI leads to the temperature increases over the upper reaches of the Yellow River and the middle and upper reaches of the Yangtze River in MIROC-ESM in winter, and over northeastern and southeastern China in MIROC-ESM-CHEM in summer, respectively (Figs. 6f and 7e). These increases are weak and insignificant. The physical processes responsible for SAI-induced cooling or warming will be discussed in the subsequent sections.

**4.2 Decomposition of SAI-induced temperature change**

We decompose the SAI-induced change in surface air temperature over China by utilizing Eqs. (1)–(4). The regionally averaged value of each term is illustrated in Fig. 8. It can be seen that SAI decreases downward net surface radiation fluxes, leading to a surface cooling of 0.30–1.45°C in summer and 0.48–2.10°C in winter over China. These decreases are partly compensated by decreased nonradiative fluxes, especially the decreased LH. The contributions of SH, $Q$, and Res are relatively small (Fig. 8a). The decomposition of downward surface radiation shows the decreases in SW$^{cs\downarrow}$ and LW$^{cs\downarrow}$ in all models. The reduced LW$^{cs\downarrow}$ dominates the deficient downward net surface radiation and decreases the temperature with magnitudes of 0.38–1.33°C in summer and 0.25–1.38°C in winter. The reduced SW$^{cs\downarrow}$ also contributes to the surface cooling, with magnitudes of 0.04–0.33°C in summer and

9

0.13–0.41°C in winter. The winter decrease in $SW^{cs\downarrow}$ is stronger than the summer one in most models. Besides, the inter-model differences in CRF and SAF changes are relatively substantial. The area-averaged results illustrate that the changes in CRF and SAF have negative and positive contributions to the SAI-induced cooling over China in most models, respectively (Fig. 8b).

The spatial patterns of SAI-induced changes in key energy-related variables over China are illustrated in Fig. 9. Under SAI forcing, changes in atmospheric temperature and water vapor lead to a general decrease in the $LW^{cs\downarrow}$. The $SW^{cs\downarrow}$, primarily related to the solar radiation scattering effect by stratospheric sulfate aerosol particles, also exhibits a coherent reduction over China. The spatial pattern of temperature change over China is primarily determined by $SW^{cl\downarrow}$ and surface albedo changes. In summer, most models exhibit increases in cloud amount, especially over northwestern and central China. The resultant decreased $SW^{cl\downarrow}$ leads to strong cooling over these regions. Conversely, northeastern and southeastern China show increased $SW^{cl\downarrow}$ and relatively weak cooling (Fig. 9d). In MIROC-ESM-CHEM, the excessive $SW^{cl\downarrow}$ (up to 8 W m$^{-2}$) offsets the clear-sky radiative effects and causes abnormal warming over most regions of eastern China (Fig. S1a). In summer, the surface albedo change due to SAI over China is relatively small. The increased surface albedo mainly occurs in the Tibetan Plateau, which contributes to local surface cooling (Fig. 9f). This may help to explain why the cloud effect is not a primary factor of temperature change over the Tibetan Plateau in summer.

In winter, a robust and coherent SAI-induced reduction in cloud cover is found over China (Fig. 9k). This reduction leads to a general increase in $SW^{cl\downarrow}$, causing the weak cooling south of the Yangtze River valley. In other areas of China, however, the change in surface albedo is the primary factor affecting the spatial pattern of temperature response under SAI forcing. The increased surface albedo leads to strong cooling, especially over northwestern and central China. However, the decreased surface albedo is found over the upper reaches of the Yellow River and the middle and upper reaches of the Yangtze River in MIROC-ESM with magnitudes greater than 3%, which results in the abnormal winter warming mentioned above (Fig. S1d). Taken together, the increased summer cloud cover and winter surface albedo lead to strong cooling, while the decreased summer cloud cover and winter surface albedo result in weak cooling, or even warming for the certain subregions and models, for instance eastern China in MIROC-ESM-CHEM and the upper reaches of the Yellow River and the middle and upper reaches of the Yangtze River in MIROC-ESM.

**4.3 Physical processes responsible for SAI-induced temperature changes**

Previous studies have illustrated that the SAI reduces the tropospheric temperature and atmospheric water vapor amount on a global scale (Kashimura et al., 2017; Visioni et al., 2018). In China, these reductions cause the decreased $LW^{cs\downarrow}$, contributing to the surface cooling primarily. We further address the potential reasons for the $SW^{cs\downarrow}$ change by using the aforementioned decomposition method. The atmospheric reflection of solar radiation increases after sulfate aerosols injection. In our study, the effect of aerosols scattering on shortwave radiation is represented as $SW_{SRM}$, which can be measured by the change in SAOD. As shown in Fig. 10, the latitudinal distributions of the calculated (used in HadGEM2-ES) and prescribed (used in BNU-ESM, CNRM-ESM1 and the MIROC-based models) SAOD changes caused by SAI in G4 display a coherent increase over China. The distribution in CanESM2 is not shown because it is a constant field according to the experimental design. The SAOD change in HadGEM2-ES is unavailable. Total aerosol optical depth is therefore considered as a reasonable alternative variable for SAOD (e.g., Bellouin et al., 2011). The national-scale increased SAOD results in a robust decrease in $SW_{SRM}$ (Figs. 11a, d), contributing to the surface cooling with magnitudes of 0.21–0.54°C in summer and 0.26–0.69°C in winter. Besides, the deficit in column-integrated water vapor reduces the atmospheric absorption of solar radiation. The resultant increased SW ($SW_{WV}$) counterbalance 37–81% and 11–48% of the reductions in $SW_{SRM}$ over China in summer and winter, respectively (Figs. 11b, e). This is the main reason why the SAI-induced winter cooling is severer than the summer level.

As discussed in Sect. 4.2, the spatial patterns of summer and winter temperature changes over China are mainly determined by the $SW^{cl\downarrow}$ and surface albedo, respectively. Generally, the SAI-induced decrease in LH flux reduces the low cloud cover, resulting in the positive change in $SW^{cl\downarrow}$ (Figs. 11c, f). Through this process, the significantly decreased LH over northeastern and southeastern China causes the abnormal summer warming in MIROC-ESM-CHEM (Fig. S1c). However, in summer, the effect of LH is partly offset by the SAI-induced moisture convergence at the troposphere in most models. The resultant increased cloud cover enhances the surface cooling over northwestern and central China (Fig. 11h). The change in surface albedo is closely related to land surface conditions. The SAI-induced cooling can be amplified by increased snow cover or sea ice (e.g., Schmidt et al., 2012). Considering surface albedo can be reasonably described as a linear function of snow cover

293  fraction (Qu and Hall, 2007; Li et al., 2016), we further investigate the spatial pattern of changes in

294  snow cover fraction, and find that matches with surface albedo over China (Figs. 11i, l; note that model

295  data are not available for HadGEM2-ES). Under SAI forcing, the increased snow cover mainly occurs

296  over the Tibetan Plateau in summer, and over northwestern and central China in winter. The enlarged

297  snow cover fraction gives rise to SW decrease at the surface, which in turn has a positive feedback on

298  surface cooling. Furthermore, the SAI-induced abnormal winter warming in MIROC-ESM is also

299  associated with the decreased snow cover over the upper reaches of the Yellow River and the middle

300  and upper reaches of the Yangtze River (Fig. S1e).

## 5 Conclusions and discussion

302      We analyze the surface air temperature response to SAI forcing over China based on the

303  simulations of the G4 experiment and RCP4.5 scenario by using six GCMs (BNU-ESM, CanESM2,

304  CNRM-ESM1, HadGEM2-ES, MIROC-ESM and MIROC-ESM-CHEM). We also discuss the

305  physical processes involved in the temperature response from a surface energy budget perspective. The

306  main conclusions are summarized as follows.

307      (1) All selected models can well reproduce the present climatological surface air temperature over

308  China in both summer and winter. Although the SAI in the G4 experiment leads to a surface cooling

309  over China, the climatological temperature in G4 is still higher than the present level. During the

310  simulation period of 2030–2069, SAI leads to a national-scale cooling over China in all models.

311  Regionally, the multi-model mean cooling is 0.64°C in summer and 0.80°C in winter, respectively. The

312  SAI-induced temperature change varies among models, regions and seasons.

313      (2) The decomposition of temperature change based on the surface energy budget indicates that

314  the SAI-induced surface cooling over China is dominated by the robust decrease in downward clear-

315  sky radiation fluxes (particularly in downward clear-sky longwave radiation flux), and associated with

316  the changes in cloud effective forcing and surface albedo feedback. The shortwave radiative effect of

317  clouds and the surface albedo feedback determine the spatial pattern of temperature change, which are

318  somewhat model-dependent and display a level of regional and seasonal discrepancies.

319      (3) Under SAI forcing, the decreased downward clear-sky longwave radiation is mainly due to

320  the decreased tropospheric temperature and water vapor amount, and the decreased downward clear-

sky shortwave radiation is mainly contributed by the aerosol scattering effect over China. The decreased latent heat flux generally reduces the cloud cover over China, but the change in summer cloud cover is closely associated with the anomalous tropospheric moisture flux convergence. The negative surface albedo feedback related to increased snow cover fraction also amplifies the surface cooling, especially over the Tibetan Plateau in summer, and over northwestern and central China in winter. The results above are summarized schematically in Fig. 12.

Finally, note that equatorial stratospheric sulfate aerosol geoengineering can induce global cooling through the transport of Brewer-Dobson circulation, and also leads to regional inequities in the temperature response due to the complicated processes of aerosol microphysics and stratospheric transport (Kravitz et al., 2019). This means that some areas will face more severe climatic disasters if this kind of geoengineering is implemented. To solve this issue, certain SAI experiments based on the injection at multiple locations have been proposed, such as the stratospheric aerosol geoengineering large ensemble project (GLENS) using CESM1(WACCM) (Tilmes et al., 2018). In addition, the uncertainty of the regional climate response to SAI is closely related to the reliability of the models (Irvine et al., 2016). It has been indicated that the CMIP6 GCMs perform better in simulating the temperature over China than their CMIP5 counterparts (Jiang et al., 2020). Therefore, the climate response to SAI geoengineering over China based on state-of-the-art GCM experiments merits further study.

*Code and data availability*. The dataset used in this study can be accessed with the following links: https://esgf-node.llnl.gov/search/cmip5/.

*Author contributions*. Dabang Jiang and Zhaochen Liu designed and performed the research. Zhaochen Liu and Xianmei Lang analyzed the data. Zhaochen Liu and Dabang Jiang wrote the manuscript. All authors contributed to this study.

*Competing interests*. The authors declare no competing interests.

## References

Arora, V. K., Scinocca, J. F., Boer, G. J., Christian, J. R., Denman, K. L., Flato, G. M., Kharin, V. V., Lee, W. G., and Merryfield, W. J.: Carbon emission limits required to satisfy future representative concentration pathways of greenhouse gases, Geophys. Res. Lett., 38, L05805, https://doi.org/10.1029/2010GL046270, 2011.

Bala, G., Duffy, P. B., and Taylor, K. E.: Impact of geoengineering schemes on the global hydrological cycle, Proc. Natl. Acad. Sci. U. S. A., 105, 7664–7669, https://doi.org/10.1073/pnas.0711648105, 2008.

Bellouin, N., Rae, J., Jones, A., Johnson, C., Haywood, J., and Boucher, O.: Aerosol forcing in the Climate Model Intercomparison Project (CMIP5) simulations by HadGEM2-ES and the role of ammonium nitrate, J. Geophys. Res., 116, D20206, https://doi.org/10.1029/2011JD016074, 2011.

Bluth, G. J., Doiron, S. D., Schnetzler, C. C., Krueger, A. J., and Walter, L. S.: Global tracking of the $SO_2$ clouds from the June, 1991 Mount Pinatubo eruptions, Geophy. Res. Lett., 19, 151–154, https://doi.org/10.1029/91GL02792, 1992.

Budyko, M. I.: Climatic Changes, American Geophysical Union, Washington, DC, 244 pp., https://doi.org/10.1029/SP010, 1977.

Caldeira, K., Bala, G., and Cao, L.: The science of geoengineering. Annu. Rev. Earth Planet. Sci., 41, 231–256, https://doi.org/10.1146/annurev-earth-042711-105548, 2013.

Cao, L., Gao, C. C., and Zhao, L. Y.: Geoengineering: Basic science and ongoing research efforts in China, Adv. Clim. Chang. Res., 6, 188–196, http://dx.doi.org/10.1016/j.accre.2015.11.002, 2015.

Collins, W. J., Bellouin, N., Doutriaux-Boucher, M., Gedney, N., Halloran, P., Hinton, T., Hughes, J., Jones, C. D., Joshi, M., Liddicoat, S., Martin, G., O'Connor, F., Rae, J., Senior, C., Sitch, S.,

Totterdell, I., Wiltshire, A., and Woodward, S.: Development and evaluation of an earth-system model – HadGEM2, Geosci. Model Dev., 4, 1051–1075, https://doi.org/10.5194/gmd-4-1051-2011, 2011.

Crutzen, P. J.: Albedo enhancement by stratospheric sulfur injections: A contribution to resolve a policy dilemma? Clim. Change, 77, 211–220, https://doi.org/10.1007/s10584-006-9101-y, 2006.

Duan, L., Cao, L., Bala, G., and Caldeira, K.: Climate response to pulse versus sustained stratospheric aerosol forcing, Geophys. Res. Lett., 46, 8976–8984, https://doi.org/10.1029/2019GL083701, 2019.

Donohoe, A., and Battisti, D. S.: Atmospheric and surface contributions to planetary albedo, J. Clim., 24, 4402–4418, https://doi.org/10.1175/2011JCLI3946.1, 2011.

Eastham, S. D., Weisenstein, D. K., Keith, D. W., and Barrett, S. R.: Quantifying the impact of sulfate geoengineering on mortality from air quality and UV-B exposure, Atmos. Environ., 187, 424–434, https://doi.org/10.1016/j.atmosenv.2018.05.047, 2018.

Gong, T., Feldstein, S., and Lee, S.: The role of downward infrared radiation in the recent Arctic winter warming trend, J. Clim., 30, 4937–4949, https://doi.org/10.1175/JCLI-D-16-0180.1, 2017.

Irvine, P. J., Kravitz, B., Lawrence, M. G., and Muri, H.: An overview of the Earth system science of solar geoengineering, Wiley Interdiscip. Rev.-Clim. Chang., 7, 815–833, https://doi.org/10.1002/wcc.423, 2016.

Irvine, P. J., Emanuel, K., He, J., Horowitz, L. W., Vecchi, G., and Keith, D.: Halving warming with idealized solar geoengineering moderates key climate hazards, Nat. Clim. Change, 9, 295–299, 2019.

Jarvis, A.: The magnitudes and timescales of global mean surface temperature feedbacks in climate models, Earth Syst. Dynam., 2, 213–221, https://doi.org/10.5194/esd-2-213-2011, 2011.

Ji, D., Wang, L., Feng, J., Wu, Q., Cheng, H., Zhang, Q., Yang, J., Dong, W., Dai, Y., Gong, D., Zhang, R. H., Wang, X., Liu, J., Moore, J. C., Chen, D., and Zhou, M.: Description and basic evaluation of Beijing Normal University Earth System Model (BNU-ESM) version 1, Geosci. Model Dev., 7, 2039–2064, https://doi.org/10.5194/gmd-7-2039-2014, 2014.

Ji, D., Fang, S., Curry, C., Kashimura, H., Watanabe, S., Cole, J. N., Lenton, A., Muri, H., Kravitz, B., and Moore, J.: Extreme temperature and precipitation response to solar dimming and stratospheric aerosol geoengineering, Atmos. Chem. Phys., 18, 10133–10156,

404           https://doi.org/10.5194/acp-18-10133-2018, 2018.

405   Jiang, D., Tian, Z., and Lang, X.: Reliability of climate models for China through the IPCC third to

406           fifth assessment reports, Int. J. Climatol., 36, 1114–1133, https://doi.org/10.1002/joc.4406, 2016.

407   Jiang, D., Hu, D., Tian, Z., and Lang, X.: Differences between CMIP6 and CMIP5 models in simulating

408           climate over China and the East Asian monsoon, Adv. Atmos. Sci., 37, 1102–1118,

409           https://doi.org/10.1007/s00376-020-2034-y, 2020.

410   Jones, A., Haywood, J. M., Alterskjær, K., Boucher, O., Cole, J. N., Curry, S., Charles, L., Irvine, P. J.,

411           Ji, D., Kravitz, B., Egill-Kristjánsson, J., Moore, J. C., Niemeier, U., Robock, A., Schmidt, H.,

412           Singh, B., Tilmes, S., Watanabe, S., and Yoon, J.-H.: The impact of abrupt suspension of solar

413           radiation management (termination effect) in experiment G2 of the Geoengineering Model

414           Intercomparison Project (GeoMIP), J. Geophys. Res.-Atmos., 118, 9743–9752,

415           https://doi.org/10.1002/jgrd.50762, 2013.

416   Jones, A. C., Hawcroft, M. K., Haywood, J. M., Jones, A., Guo, X., and Moore, J. C.: Regional climate

417           impacts of stabilizing global warming at 1.5 K using solar geoengineering, Earths Future, 6, 230–

418           251, https://doi.org/10.1002/2017EF000720, 2018.

419   Kashimura, H., Abe, M., Watanabe, S., Sekiya, T., Ji, D., Moore, J. C., Cole, J. N., and Kravitz, B.:

420           Shortwave radiative forcing, rapid adjustment, and feedback to the surface by sulfate

421           geoengineering: Analysis of the Geoengineering Model Intercomparison Project G4 scenario,

422           Atmos. Chem. Phys., 17, 3339–3356, https://doi.org/10.5194/acp-17-3339-2017, 2017.

423   Kravitz, B., Robock, A., Boucher, O., Schmidt, H., Taylor, K. E., Stenchikov, G., and Schulz, M.: The

424           Geoengineering Model Intercomparison Project (GeoMIP), Atmos. Sci. Lett., 12, 162–167,

425           https://doi.org/10.1002/asl.316, 2011.

426   Kravitz, B., Robock, A., Forster, P. M., Haywood, J. M., Lawrence, M. G., and Schmidt, H.: An

427           overview of the Geoengineering Model Intercomparison Project (GeoMIP), J. Geophys. Res.-

428           Atmos., 118, 13103–13107, https://doi.org/10.1002/2013JD020569, 2013a.

429   Kravitz, B., Rasch, P. J., Forster, P. M., Andrews, T., Cole, J. N., Irvine, P. J., Ji, D., Kristjánsson, J.,

430           Moore, J. C., Muri, H., Niemeier, U., Robock, A., Singh, B., Tilmes, S., Watanabe, S., and Yoon,

431           J.-H.: An energetic perspective on hydrological cycle changes in the Geoengineering Model

432           Intercomparison Project, J. Geophys. Res.-Atmos., 118, 13087–13102,

433           https://doi.org/10.1002/2013JD020502, 2013b.

Kravitz, B., MacMartin, D. G., Robock, A., Rasch, P. J., Ricke, K. L., Cole, J. N., Curry, C. L., Irvine, P. J., Ji, D., Keith, D. W., Kristjánsson, J. E., Moore, J. C., Muri, H., Singh, B., Tilmes, S., Watanabe, S., Yang, S., and Yoon, J. H.: A multi-model assessment of regional climate disparities caused by solar geoengineering, Environ. Res. Lett., 9, 074013, https://doi.org/10.1088/1748-9326/9/7/074013, 2014.

Kravitz, B., Robock, A., Tilmes, S., Boucher, O., English, J. M., Irvine, P. J., Jones, A., Lawrence, M. G., MacCracken, M., Muri, H., Moore, J. C., Niemeier, U., Phipps, S. J., Sillmann, J., Storelvmo, T., Wang, H., and Watanabe, S.: The Geoengineering Model Intercomparison Project Phase 6 (GeoMIP6): simulation design and preliminary results, Geosci. Model Dev., 8, 3379–3392, https://doi.org/10.5194/gmd-8-3379-2015, 2015.

Kravitz, B., MacMartin, D. G., Tilmes, S., Richter, J. H., Mills, M. J., Cheng, W., Dagon, K., Glanville, A. S., Lamarque, J.-F., Simpson, I. R., Tribbia, J., and Vitt, F.: Comparing surface and stratospheric impacts of geoengineering with different $SO_2$ injection strategies, J. Geophys. Res.-Atmos., 124, 7900–7918, https://doi.org/10.1029/2019JD030329, 2019.

Latham, J.: Control of global warming? Nature, 347, 339–340, https://doi.org/10.1038/347339b0, 1990.

Li, Y., Wang, T., Zeng, Z., Peng, S., Lian, X., and Piao, S.: Evaluating biases in simulated land surface albedo from CMIP5 global climate models, J. Geophys. Res.-Atmos., 121, 6178–6190, https://doi.org/10.1002/2016JD024774, 2016.

Lu, J., and Cai, M.: Seasonality of polar surface warming amplification in climate simulations, Geophys. Res. Lett., 36, L16704, https://doi.org/10.1029/2009GL040133, 2009.

Matthews, H. D., and Caldeira, K.: Transient climate–carbon simulations of planetary geoengineering, Proc. Natl. Acad. Sci. U. S. A., 104, 9949–9954, https://doi.org/10.1073/pnas.0700419104, 2007.

Mitchell, D. L., and Finnegan, W.: Modification of cirrus clouds to reduce global warming, Environ. Res. Lett., 4, 045102, https://doi.org/10.1088/1748-9326/4/4/045102, 2009.

Qu, X., and Hall, A.: What controls the strength of snow-albedo feedback? J. Clim., 20, 3971–3981, https://doi.org/10.1175/JCLI4186.1, 2007.

Raible, C. C., Brönnimann, S., Auchmann, R., Brohan, P., Frölicher, T. L., Graf, H. F., Jones, P., Luterbacher, J., Muthers, S., Neukom, R., Robock, A., Self, S., Sudrajat, A., Timmreck, C., and Wegmann, M.: Tambora 1815 as a test case for high impact volcanic eruptions: Earth system effects, Wiley Interdiscip. Rev.-Clim. Chang., 7, 569–589, https://doi.org/10.1002/wcc.407, 2016.

Rasch, P. J., Crutzen, P. J., and Coleman, D. B.: Exploring the geoengineering of climate using stratospheric sulfate aerosols: The role of particle size, Geophys. Res. Lett., 35, L02809, https://doi.org/10.1029/2007GL032179, 2008.

Ricke, K. L., Moreno-Cruz, J. B., and Caldeira, K.: Strategic incentives for climate geoengineering coalitions to exclude broad participation, Environ. Res. Lett., 8, 014021, https://doi.org/10.1088/1748-9326/8/1/014021, 2013.

Robiou du Pont, Y., and Meinshausen, M.: Warming assessment of the bottom-up Paris Agreement emissions pledges, Nat. Commun., 9, 4810, https://doi.org/10.1038/s41467-018-07223-9, 2018.

Robock, A., Oman, L., and Stenchikov, G. L.: Regional climate responses to geoengineering with tropical and Arctic $SO_2$ injections, J. Geophys. Res., 113, D16, https://doi.org/10.1029/2008JD010050, 2008.

Robock, A.: Stratospheric aerosol geoengineering, AIP Conf. Proc., 1652, 183–197, https://doi.org/10.1063/1.4916181, 2015.

Sato, M.: Forcings in GISS climate model: Stratospheric aerosol optical thickness, available at: https://data.giss.nasa.gov/modelforce/strataer/, 2006. (last access: April 2021)

Schmidt, H., Alterskjær, K., Bou Karam, D., Boucher, O., Jones, A., Kristjánsson, J. E., Niemeier, U., Schulz, M., Aaheim, A., Benduhn, F., Lawrence, M., and Timmreck, C.: Solar irradiance reduction to counteract radiative forcing from a quadrupling of $CO_2$: Climate responses simulated by four earth system models, Earth Syst. Dynam., 3, 63–78, https://doi.org/10.5194/esd-3-63-2012, 2012.

Seifritz, W.: Mirrors to halt global warming, Nature, 340, 603, https://doi.org/10.1038/340603a0, 1989.

Séférian, R., Delire, C., Decharme, B., Voldoire, A., David, S. Y. M., Chevallier, M., Saint-Martin, D., Aumont, O., Calvet, J.-C., Carrer, D., Douville, H., Franchistéguy, L., Joetzjer, E., and Sénési, S.: Development and evaluation of CNRM Earth system model – CNRM-ESM1, Geosci. Model Dev., 9, 1423–1453, https://doi.org/10.5194/gmd-9-1423-2016, 2016.

Sudo, K., Takahashi, M., Kurokawa, J., and Akimoto, H.: CHASER: A global chemical model of the troposphere: 1. Model description, J. Geophys. Res., 107, 4339, https://doi.org/10.1029/2001JD001113, 2002.

Sun, W., Wang, B., Chen, D., Gao, C., Lu, G., and Liu, J.: Global monsoon response to tropical and Arctic stratospheric aerosol injection, Clim. Dyn., 55, 2107–2121,

494        https://doi.org/10.1007/s00382-020-05371-7, 2020.

495  Taylor, K. E.: Summarizing multiple aspects of model performance in a single diagram, J. Geophys.

496        Res.-Atmos., 106, 7183–7192, https://doi.org/10.1029/2000JD900719, 2001.

497  Taylor, K. E., Stouffer, R. J., and Meehl, G. A.: An overview of CMIP5 and the experiment design,

498        Bull. Amer. Meteorol. Soc., 93, 485–498, https://doi.org/10.1175/BAMS-D-11-00094.1, 2012.

499  Tilmes, S., Müller, R., and Salawitch, R.: The sensitivity of polar ozone depletion to proposed

500        geoengineering schemes, Science, 320, 1201–1204, https://doi.org/10.1126/science.1153966,

501        2008.

502  Tilmes, S., Fasullo, J., Lamarque, J. F., Marsh, D. R., Mills, M., Alterskjær, K., Muri, H., Kristjánsson,

503        J. E., Boucher, O., Schulz, M., Cole, J. N. S., Curry, C. L., Jones, A., Haywood, J., Irvine, P. J.,

504        Ji, D., Moore, J. C., Karam, D. B., Kravitz, B., Rasch, P. J., Singh, B., Yoon, J.-H., Niemeier, U.,

505        Schmidt, H., Robock, A., Yang, S., and Watanabe, S.: The hydrological impact of geoengineering

506        in the Geoengineering Model Intercomparison Project (GeoMIP), J. Geophys. Res.-Atmos., 118,

507        11036–11058, https://doi.org/10.1002/jgrd.50868, 2013.

508  Tilmes, S., Richter, J. H., Kravitz, B., MacMartin, D. G., Mills, M. J., Simpson, I. R., Glanville, A. S.,

509        Fasullo, J. T., Phillips, A. S., Lamarque, J.-F., Tribbia, J., Edwards, J., Mickelson, S., and Ghosh,

510        S.: CESM1 (WACCM) stratospheric aerosol geoengineering large ensemble project, Bull. Amer.

511        Meteorol. Soc., 99, 2361–2371, https://doi.org/10.1175/BAMS-D-17-0267.1, 2018.

512  Trenberth, K. E., and Dai, A.: Effects of Mount Pinatubo volcanic eruption on the hydrological cycle

513        as an analog of geoengineering, Geophys. Res. Lett., 34, 1438–1442,

514        https://doi.org/10.1029/2007GL030524, 2007.

515  United Nations Environment Programme.: Emissions Gap Report 2020, UNEP, Nairobi, 2020.

516  Visioni, D., Pitari, G., di Genova, G., Tilmes, S., and Cionni, I.: Upper tropospheric ice sensitivity to

517        sulfate geoengineering, Atmos. Chem. Phys., 18, 14867–14887, https://doi.org/10.5194/acp-18-

518        14867-2018, 2018.

519  Watanabe, S., Hajima, T., Sudo, K., Nagashima, T., Takemura, T., Okajima, H., Nozawa, T., Kawase,

520        H., Abe, M., Yokohata, T., Ise, T., Sato, H., Kato, E., Takata, K., Emori, S., and Kawamiya, M.:

521        MIROC-ESM 2010: Model description and basic results of CMIP5-20c3m experiments, Geosci.

522        Model Dev., 4, 845–872, https://doi.org/10.5194/gmd-4-845-2011, 2011.

523  Wigley, T. M. L.: A combined mitigation/geoengineering approach to climate stabilization, Science,

524          314, 452–454, https://doi.org/10.1126/science.1131728, 2006.

525     Wu, J., and Gao, X.: A gridded daily observation dataset over China region and comparison with the

526          other datasets, Chinese J. Geophy., 56, 1102–1111, https://doi.org/10.6038/cjg20130406, 2013.

527          (in Chinese)

528 **Table 1**. Main features of climate models used in this study.

| Model | Atmospheric resolution (longitude, latitude, and vertical levels) | Ensemble number | Stratospheric aerosol | Reference |
|---|---|---|---|---|
| BNU-ESM | ~2.8° × ~2.8°, L26 | 1 | Prescribed | Ji et al., 2014 |
| CanESM2 | ~2.8° × ~2.8°, L35 | 3 | Uniform | Arora et al., 2011 |
| CNRM-ESM1 | ~1.4° × ~1.4°, L31 | 2 | Prescribed | Séférian et al., 2016 |
| HadGEM2-ES | 1.875° × 1.25°, L38 | 3 | Generated from $SO_2$ injection | Collins et al., 2011 |
| MIROC-ESM | ~2.8° × ~2.8°, L80 | 1 | Prescribed | Watanabe et al., 2011 |
| MIROC-ESM-CHEM | ~2.8° × ~2.8°, L80 | 1 | Prescribed | Watanabe et al., 2011 |

529
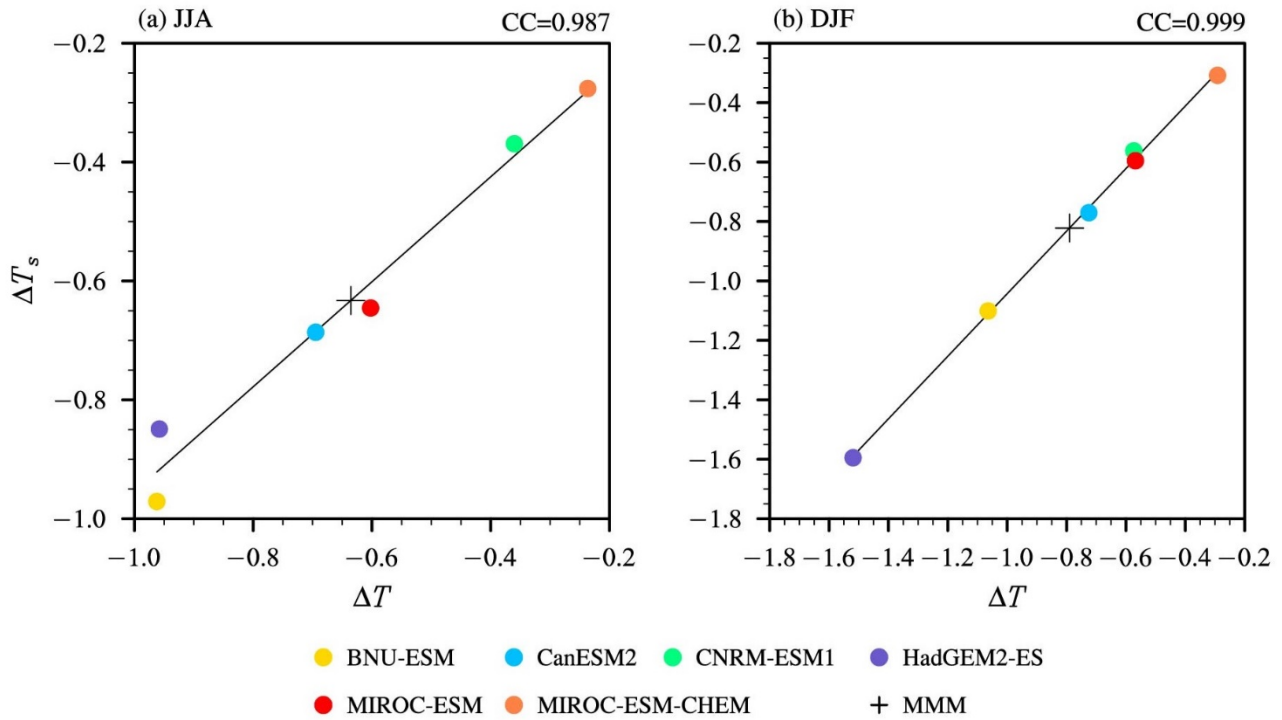
**Figure 1**. Scatter plots of relationship between changes in surface air temperature ($T$) and surface temperature ($T_s$) over China due to SAI forcing during the period of 2030–2069 in (a) summer (JJA) and (b) winter (DJF), and CC is their correlation coefficient. Scatters and cross represent individual models and their mean, respectively.
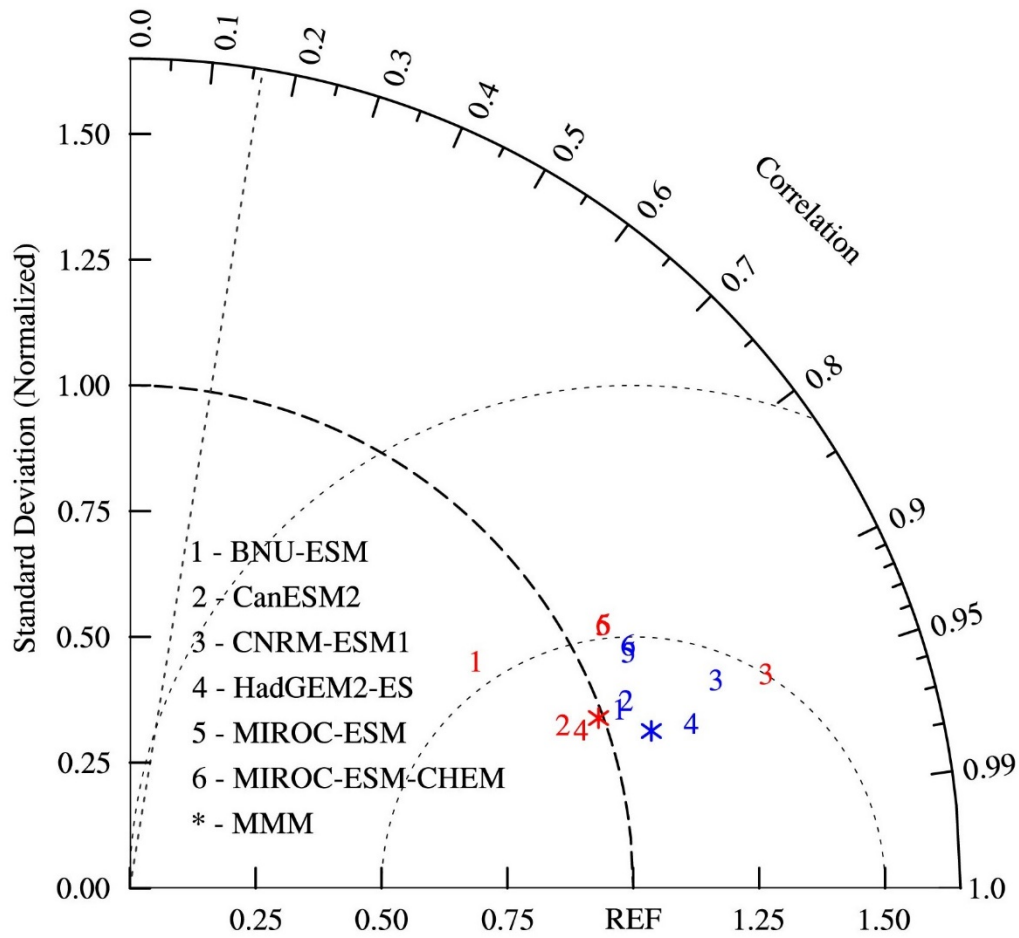
**Figure 2**. Taylor diagram of climatological summer and winter temperatures over China between the historical simulations in selected models and observation during the period of 1986–2005. Numbers represent individual models, and asterisks represent the multi-model mean. Red and blue represent summer and winter, respectively. The dotted straight line shows the 99% confidence level determined from the two-tailed Student's *t*-test.
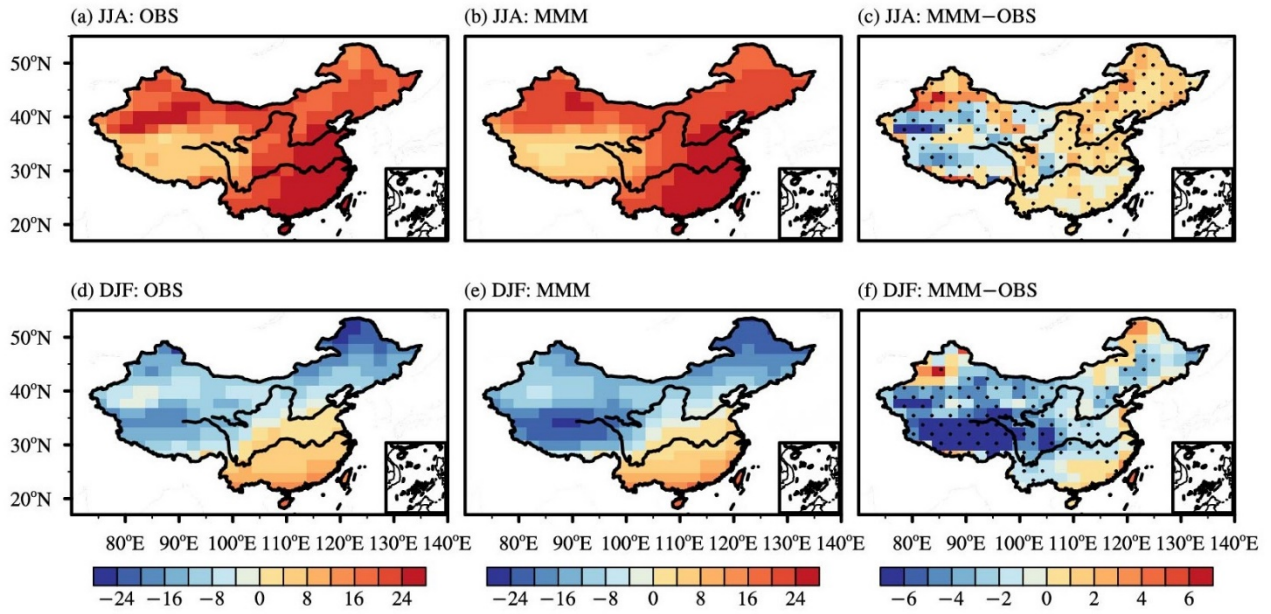
**Figure 3**. Spatial patterns of surface air temperature climatology (units: °C) over China as obtained from observation (left column; OBS), the multi-model mean (middle column; MMM), and the difference between multi-model mean and observation (right column; MMM–OBS) during the period of 1986–2005 in summer (JJA) and winter (DJF). The dots in the right column indicate areas where at least two-thirds of models share the same sign of the bias.
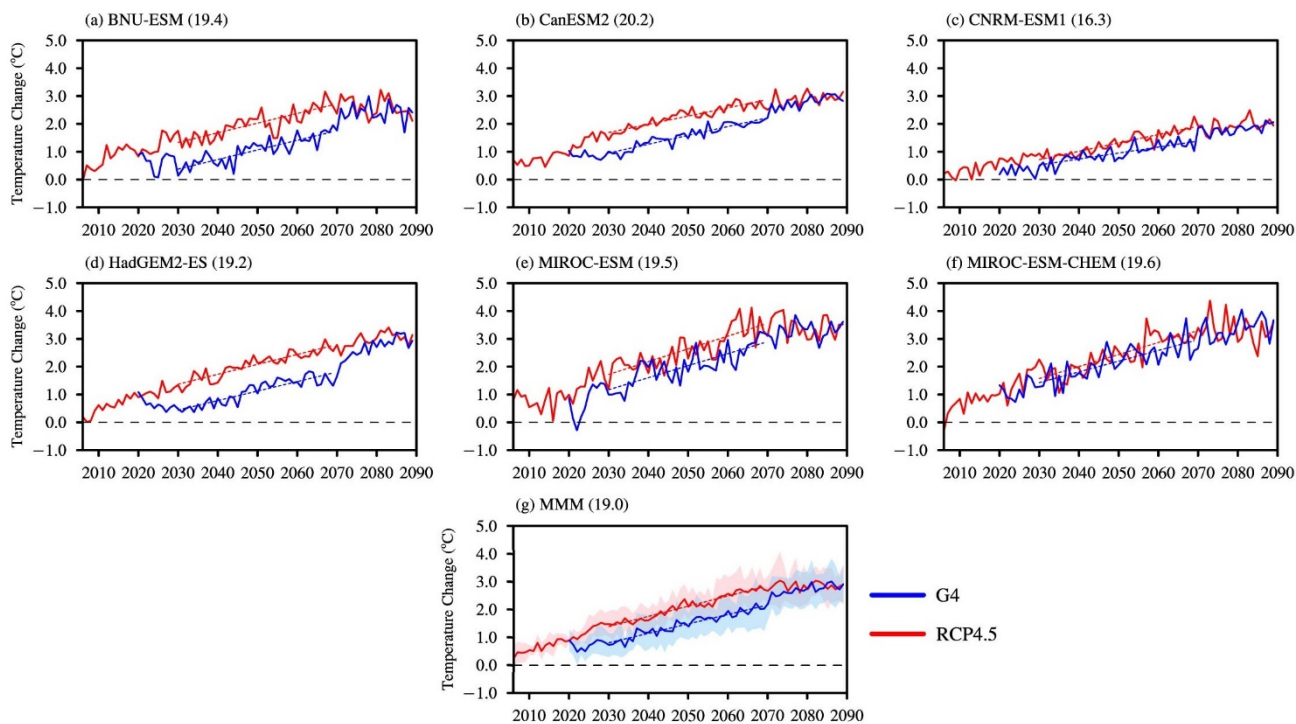
**Figure 4**. Time series of regionally averaged surface air temperature (units: °C) over China in the G4 experiment (solid blue lines) and RCP4.5 scenario (solid red lines) in summer. The values are obtained by subtracting the present climatology (mean of 1986–2005; represented in parentheses) in the historical experiment. Red and blue dashed lines represent the linear trends of G4 and RCP4.5 simulations during the period of 2030–2069, respectively. The multi-model mean (MMM) is represented at the bottom, with the shading indicating one inter-model standard deviation.
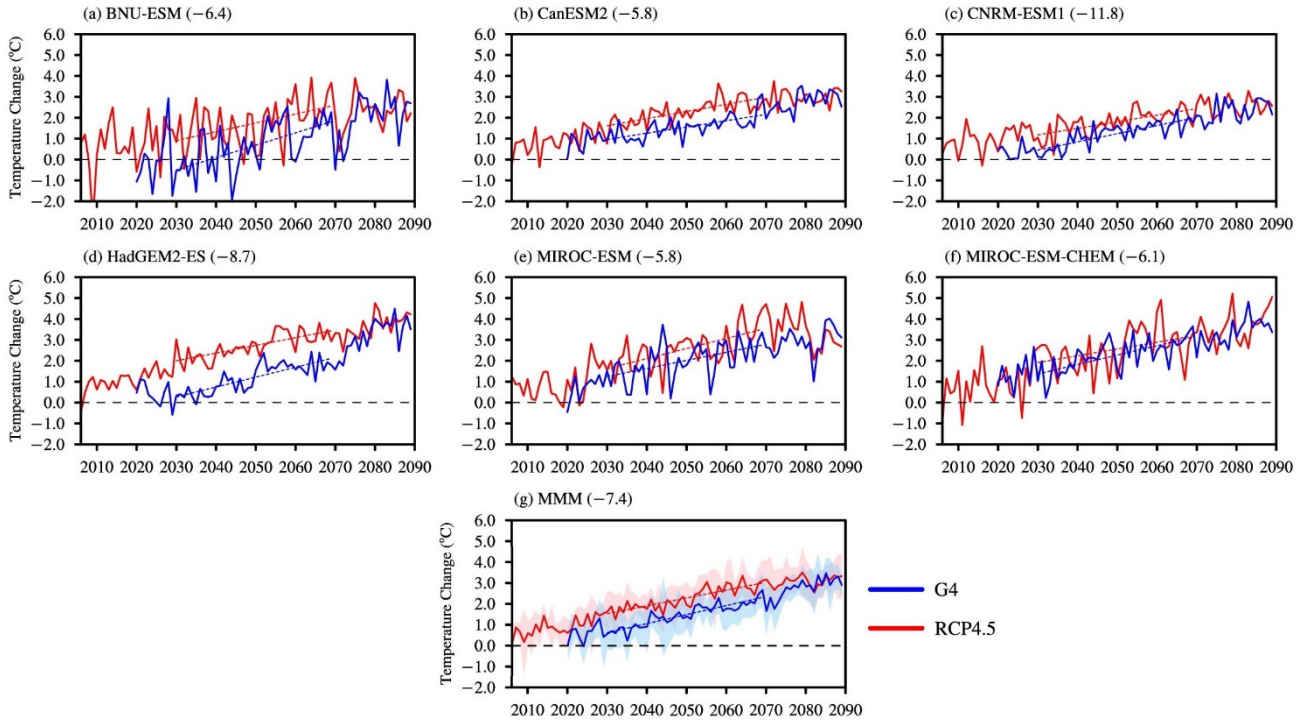
554

555    **Figure 5**. Same as Figure 4, but in winter.
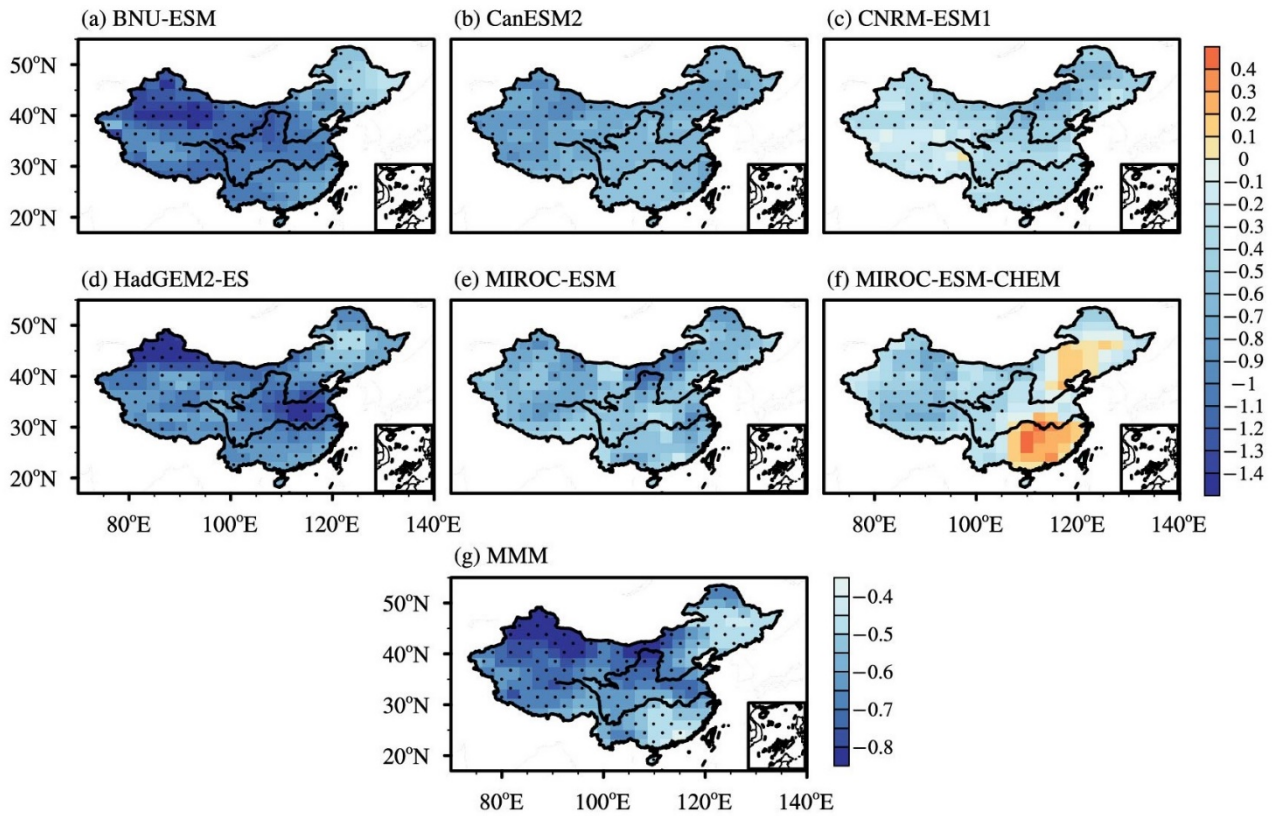
**Figure 6**. Spatial patterns of surface air temperature differences (units: °C) between G4 and RCP4.5 over China during the period of 2030–2069 in summer for (a–f) individual models and (g) the multi-model mean. The dots in (a–f) indicate areas where are statistically significant at the 90% confidence level. The dots in (g) indicate areas where at least two-thirds of models share the same sign with the multi-model mean.

562

**Figure 7**. Same as Figure 6, but in winter.
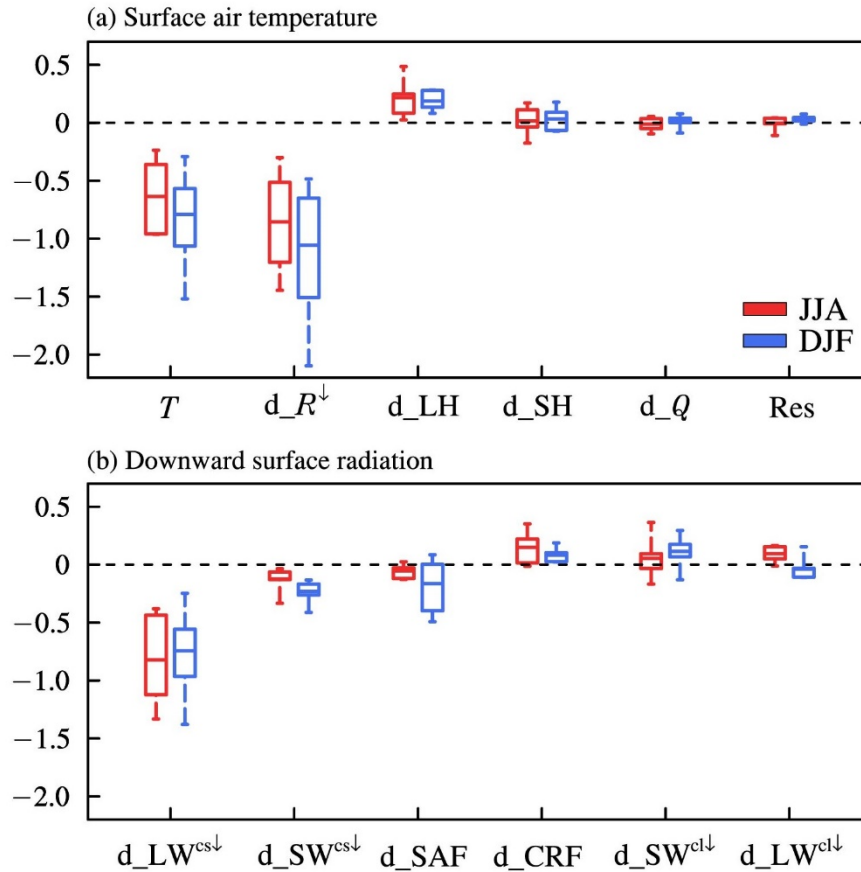
**Figure 8**. Regionally averaged SAI-induced changes in surface air temperature (*T*) and relevant terms over China during the period of 2030–2069 (units: °C). The terms include surface air temperature changes due to (a) downward net surface radiation change (d_$R^{\downarrow}$), surface latent (d_LH) and sensible (d_SH) heat flux changes, heat storage change (d_$Q$), residual term change (Res), (b) downward clear-sky surface longwave (d_$LW^{cs\downarrow}$) and shortwave (d_$SW^{cs\downarrow}$) radiation changes, surface albedo feedback change (d_SAF) and surface cloud radiative forcing change (d_CRF; including shortwave (d_$SW^{cl\downarrow}$) and longwave (d_$LW^{cl\downarrow}$) forcing changes). The error bars represent minimum and maximum values, and the boxes represent interquartile ranges among models. The middle lines present multi-model means. The red and blue bars represent values in summer and winter, respectively.
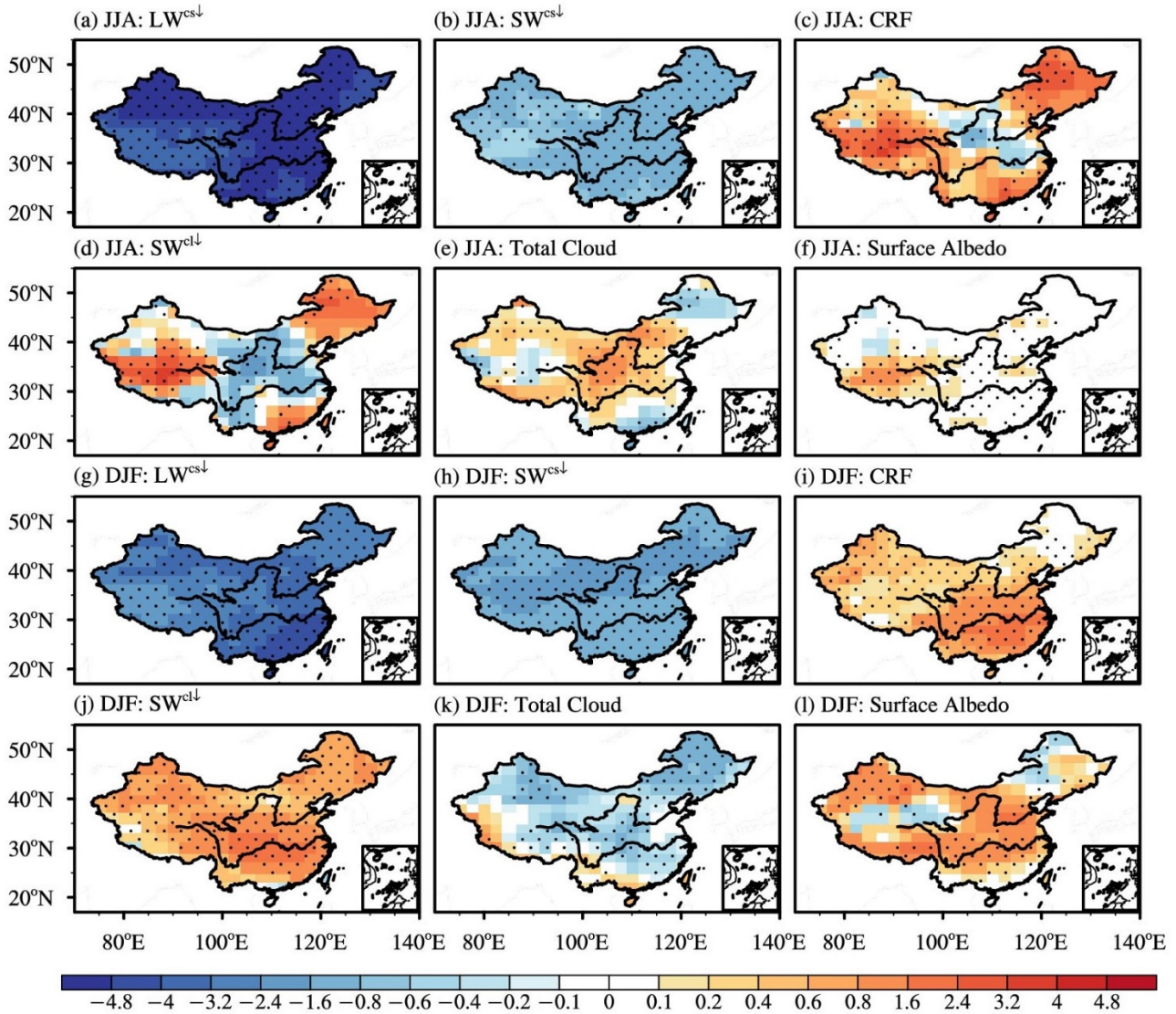
**Figure 9**. Spatial patterns of differences between G4 and RCP4.5 over China for the multi-model mean in summer (JJA) and winter (DJF): (a, g) downward clear-sky surface longwave radiation (LW$^{cs\downarrow}$); (b, h) downward clear-sky surface shortwave radiation (SW$^{cs\downarrow}$); (c, i) surface cloud radiative forcing; (d, j) downward shortwave radiative effect of clouds (SW$^{cl\downarrow}$); (e, k) total cloud cover (units: %); (f, l) surface albedo (units: %) during the period of 2030–2069. Flux is in W m$^{-2}$. The dots indicate areas where at least two-thirds of models share the same sign with the multi-model mean.
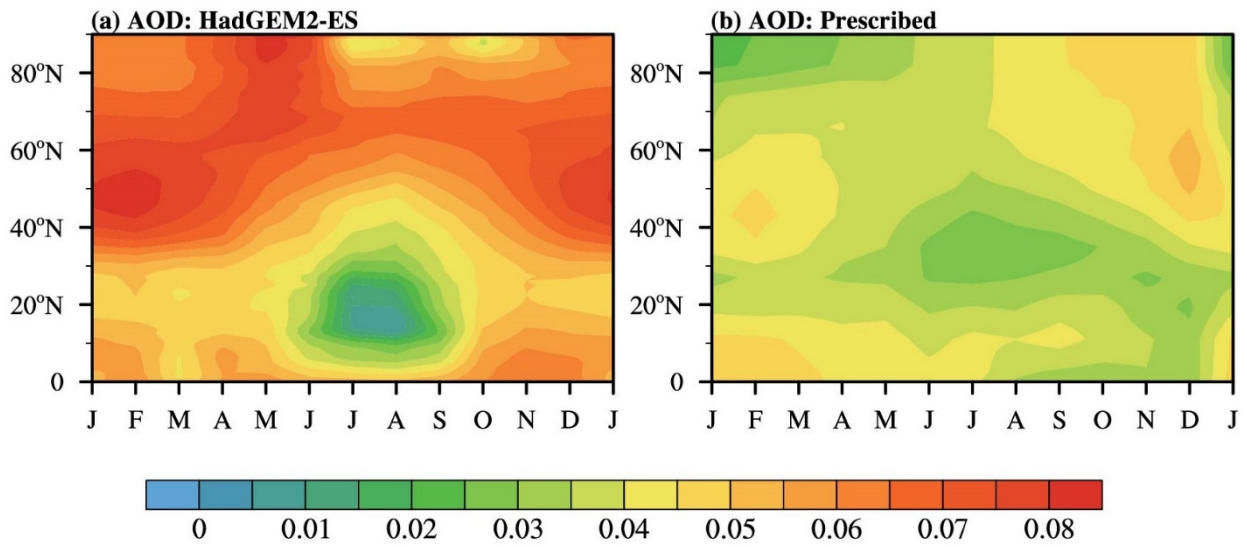
**Figure 10**. Latitudinal distributions of the calculated (a, for HadGEM2-ES) and prescribed (b, for BNU-ESM, CNRM-ESM1, and the MIROC-based models) changes in SAOD at 550 nm caused by SAI in G4 experiment over the Northern Hemisphere during the period of 2030–2069.

585
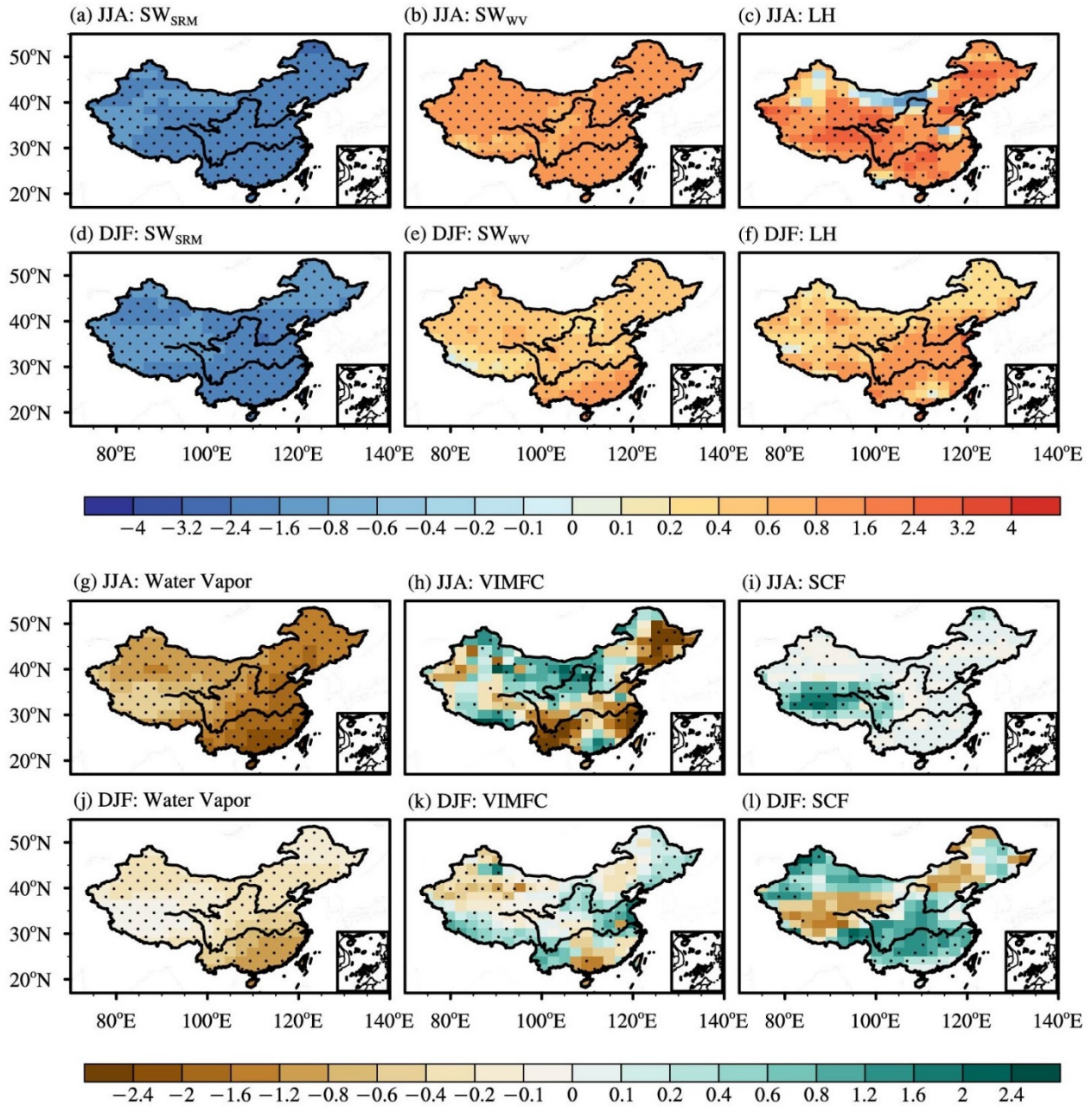
**Figure 11**. Same as Figure 9, but for the shortwave radiative effects of (a, d) solar radiation scattering change (SW$_{SRM}$) and (b, e) atmospheric water vapor amount change (SW$_{WV}$), (c, f) latent heat flux (LH), (g, j) column-integrated water vapor (units: kg m$^{-2}$), (h, k) vertically integrated moisture flux convergence (VIMFC; units: 0.1 mm d$^{-1}$), and (i, l) snow cover fraction (SCF; units: %). Flux is in W m$^{-2}$ and defined positive downward.

591
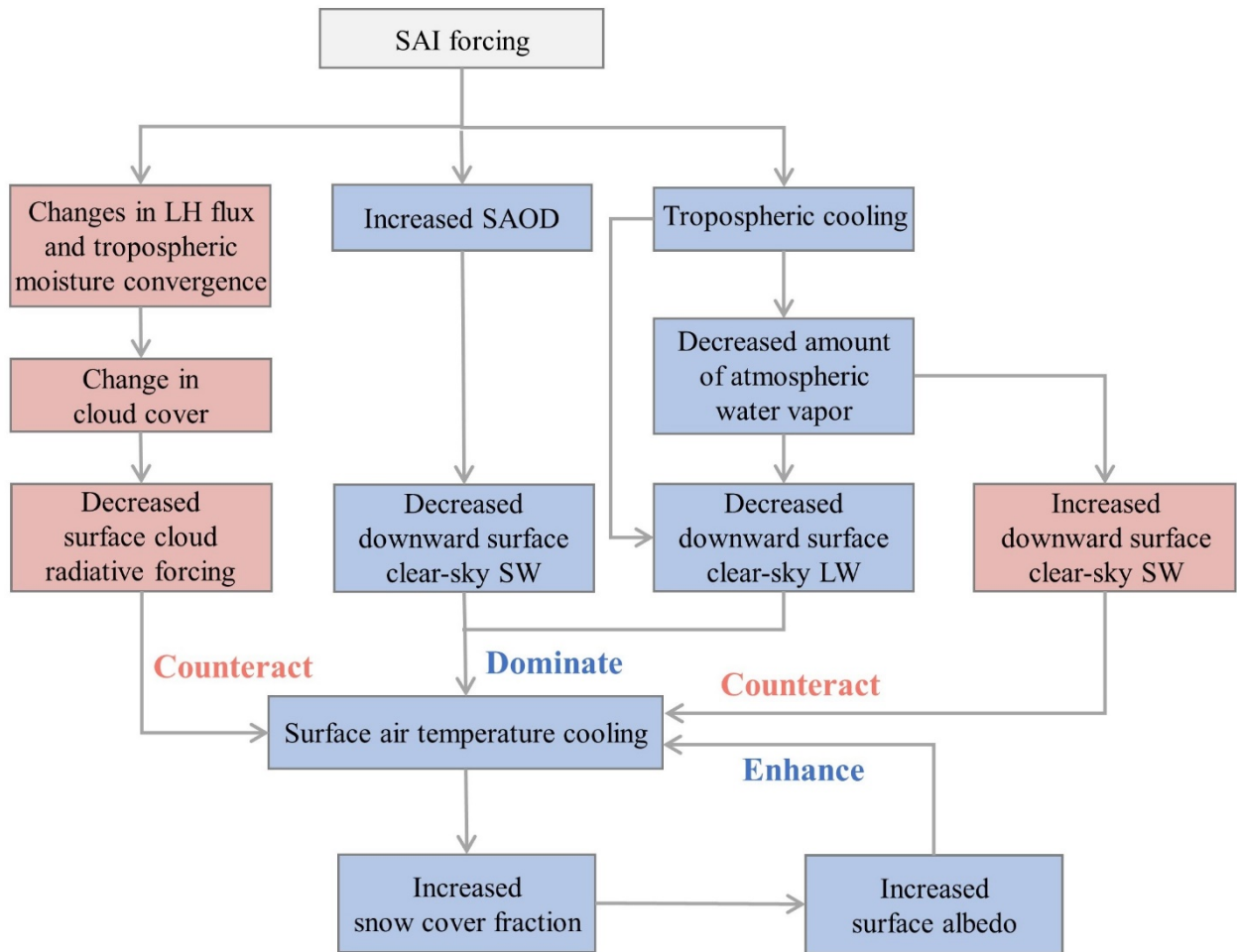
**Figure 12**. Schematic diagram illustrating how the relevant physical processes impact the downward

surface radiation changes over China in response to the SAI forcing in the G4 experiment.